RESEARCH ARTICLE

Key Points:
- The shallow mouth of small, bar-built estuaries tidally modulates nearshore ocean forcing
- While connected, infragravity motions drive fast oscillatory flow and wave setup modulates tides
- When the ocean retreats below the perched mouth, friction sets velocities and waves stop

Correspondence to:
M. E. Williams,
mewilliams@berkeley.edu

Tidally discontinuous ocean forcing in bar-built estuaries: The interaction of tides, infragravity motions, and frictional control

M. E. Williams[1,2] and M. T. Stacey[1]

[1]Department of Civil and Environmental Engineering, University of California, Berkeley, California, USA, [2]Now at National Oceanography Centre, Liverpool, UK

Abstract Shallow, bar-built estuaries on wave-dominated coasts in Mediterranean climates experience an intermittent connection to the ocean. In the presence of low streamflow, their inlets may completely close as a result of nearshore sand transport, but even in the open condition, these inlets remain constricted. Extensive field measurements in the highly salt-stratified Pescadero estuary in northern California show that the shallow mouth causes these estuaries to experience discontinuous tidal forcing. While the ocean and estuary are fully connected with near-equal water levels, tidal velocities are slow but infragravity motions in the nearshore induce large velocity oscillations within the estuary. As the ocean tide falls, infragravity forcing is cut off, because the estuarine mouth is perched above the low tide ocean water level, and ebbing velocities are set by bed friction. Observations reveal this oscillation between ocean-forced and frictionally controlled conditions characterizes and sets estuarine hydrodynamics. Additional wave setup of the lagoon emphasizes the dependence of these estuaries on nearshore ocean conditions, but the diurnal or semidiurnal retreat of the ocean below the mouth cuts off this nearshore influence so it too is tidally varying. Here we present detailed observations and a framework for understanding hydrodynamics in small, shallow bar-built estuaries.

1. Introduction

California's coast is dotted with small estuaries that drain pristine, agricultural, and highly urbanized watersheds. Formed as drowned river valleys by sea level rise after the last glacial period, these estuaries are situated behind sand barriers [*Clarke et al.*, 2014]. Similar to other bar-built estuaries found in Mediterranean climates on wave-dominated coasts worldwide, the inlets of these estuaries may become closed with sand [e.g., *Elwany et al.*, 1998; *Hanes et al.*, 2011; *Fortunato et al.*, 2014; *Ranasinghe and Pattiaratchi*, 2003]. Inlet closure is by longshore and crossshore movement of sand, thus the maintenance of the open inlet relies on sufficient ebb tidal and riverine flow [*Behrens et al.*, 2013]. Intermittently closed estuaries are geographically distributed on wave-dominated coasts which experience significant sediment transport, and in Mediterranean climates where seasonal precipitation leads to the low streamflow condition that allows for inlet closure.

Perhaps owing to intermittently closed estuaries being obviously ill suited to be harbors, little research has explored their hydrodynamics. Studies in temporarily open/closed estuaries in South Africa, intermittently closed and open lakes and lagoons in Australia, and intermittently closed estuaries in California have focused on geomorphic change [e.g., *Baldock et al.*, 2008; *Rich and Keller*, 2013], though limited measurements provide some insight into the hydrodynamic processes. Tides are typically highly attenuated in these estuaries [e.g., *Ranasinghe and Pattiaratchi*, 1999; *Gale et al.*, 2007]. Salt movement is shown to be frontal, and estuaries are likely highly salt stratified [*Largier and Taljaard*, 1991]. Previous observations have looked at overall circulation patterns of an estuary on seasonal scales, leaving the effects of short-term processes like a changing wave climate and spring-neap cycle under described.

Sparse hydrodynamic characterizations of intermittently closed estuaries exist, but relevant processes are described in other contexts. The mouth or inlets of these systems cross beaches with active wave environments [see *Mei and Liu*, 1993; *Battjes*, 1988; *Holman*, 1981]. Wave setup observed in lagoonal estuaries [e.g., *Malhadas et al.*, 2009] may be analogous to similar setup on coral reef lagoons [e.g., *Becker et al.*, 2014], and
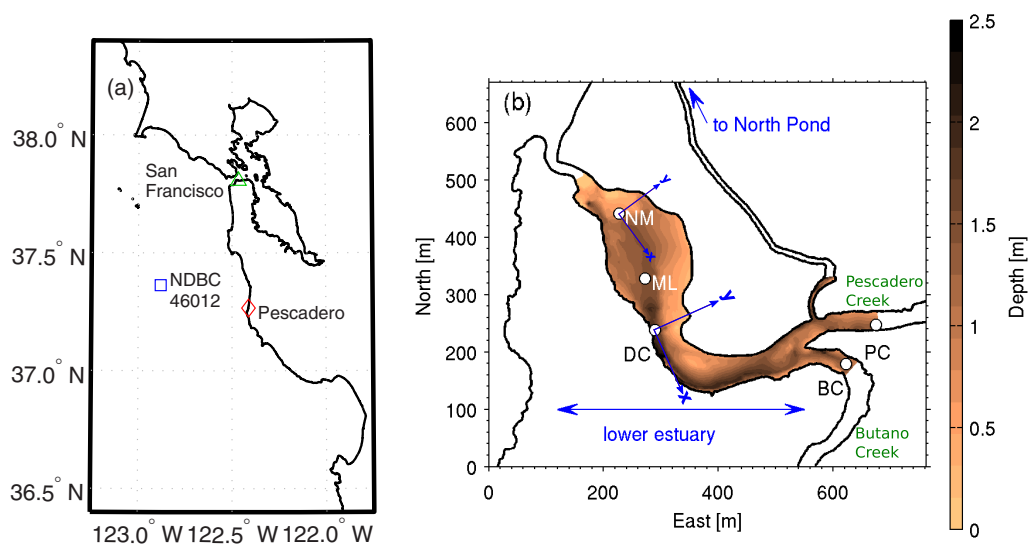
Figure 1. (a) The Pescadero estuary is located on the California coast between Monterey and San Francisco Bays. The location of sensors referenced for tidal and wave conditions is shown with a green triangle and blue square, respectively. (b) The coastline and depth at high tide in the Pescadero estuary and the locations of pressure and velocity moorings (NM: Near Mouth, ML: Mid-Lagoon, DC: Deep Channel, PC: Pescadero Creek, and BC: Butano Creek). Pescadero Creek flows into the lower estuary from the northeast, and Butano Creek from the south. The narrow channel connects the estuary to a northern pond through culverts. The coordinate system is flood positive and follows the thalweg, as depicted at DC and NM.

wave-driven flow seen on these reefs [*Monismith*, 2007; *Nwogu and Bemirbilek*, 2010] may also be important in lagoonal estuaries.

Here we present results of extensive field observations in the Pescadero estuary of northern California aimed at characterizing open-state hydrodynamics of small bar-built estuaries with intermittent connections to the ocean. The site and data collection are described, followed by a presentation of tidally discontinuous hydrodynamics. For much of the tidal cycle, the estuary is under the influence of tides and infragravity motions from the nearshore. At low tides, the nearshore influence is cut off and the estuary transitions to a draining reservoir controlled by bed friction. These dynamics exist on a background of wave-induced water level setup. Energetic implications of infragravity motions and longer-term variability are then discussed.

2. Experimental Site and Conditions

2.1. Site Description

The mouth of the Pescadero estuary is located on the California coast midway between the Golden Gate and the northern extent of Monterey Bay (Figure 1a). To the north, the Pescadero State Beach is the southern extent of approximately 10 km of sandy beach with three other small inlets. Migration of the inlet is common in this type of estuary [e.g., *Behrens et al.*, 2013], but migration of the Pescadero inlet is constrained by a rocky cliff to the south (Figure 2). The inlet is approximately 100 m long, and opens into a shallow lagoonal estuary (Figure 1b). The inlet size and shape vary as sand is eroded or built up on seasonal, spring-neap, and tidal time scales, but it remains approximately 10 m wide in its open state. At low tidal heights, flow is constrained to a sandy channel cut by ebbing tides, while at higher tidal levels flooding tidal and wave-driven flow also washes over the flatter beach. A cartoon schematic depicting the tidal range at the mouth ($\eta_{tide,mouth}$) with corresponding photographs from the Pescadero estuary are shown in Figure 2.

The lower estuary, downstream of the confluence of two creeks, has a maximum high tide depth of approximately 2.7 m in the deep channel 350 m upstream from the mouth (Figure 1b) and maximum spring tidal range of 1.4 m. The mouth of this estuary typically closes with sand between August and October due to nearshore sediment transport and reopens with the start of the California rainy season in November. During water year 2012, the first year of the current California drought, the mouth closed and opened several times, as low freshwater discharge was overwhelmed by nearshore sand transport. The inlet did not remain open
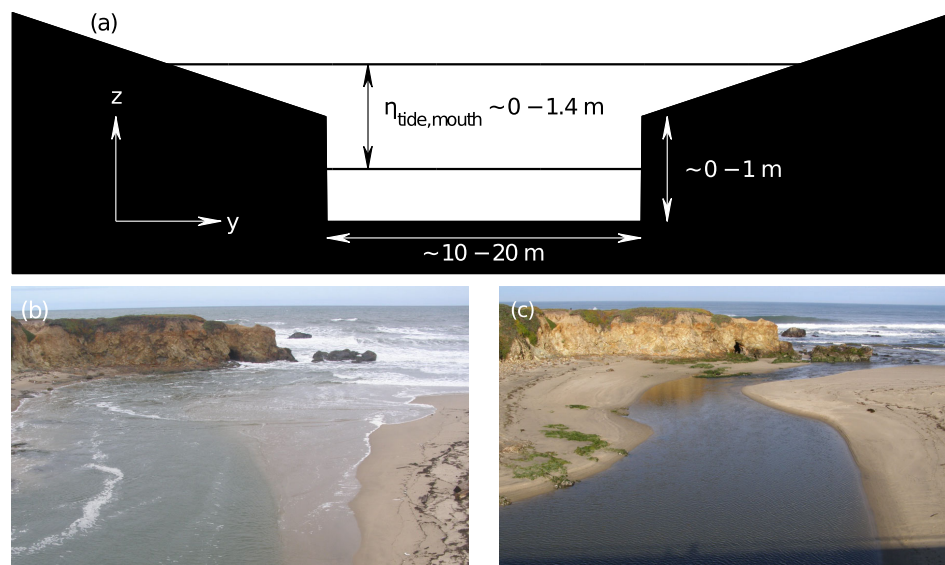
Figure 2. (a) The channelization of the inlet changes with water level, as depicted by the cartoon diagram. (b) A photograph of the mouth of the Pescadero estuary shows that at high tide, water can wash across the beach. (c) At low water, the inlet is channelized and flow is laterally restricted. The retreat of the swash zone from the inlet is also apparent. These photographs are taken facing west from the bridge crossing the Pescadero inlet.

for an extended period until early March 2012. Results presented here are exclusively from the open inlet state of the estuary.

Two creeks, the Pescadero and Butano, connect 700 m upstream of the mouth of the Pescadero estuary. Butano Creek meanders through extensive salt marsh while Pescadero Creek remains more channeled and riverine up to the confluence. Upstream of the confluence, a channel connects a shallow pond to Pescadero Creek through dilapidated culverts, installed as part of a restoration project (Figure 1b). The presence of the North Pond likely influences the inlet dynamics by increasing the tidal prism, but due to very limited connectivity through small culverts, we neglect its effect on hydrodynamics.

The Pescadero watershed covers 210 km^2 in the coastal Santa Cruz mountains. A USGS gauge (11162500), 8.5 km upstream of the mouth captures 57% of the watershed. Unaccounted for freshwater diversions exist due to agriculture in the watershed, but freshwater flow into the estuary, Q_R, is approximated by scaling the gauged freshwater discharge, $Q_{R,G}$, by the entire watershed area. The rainfall-dominated coastal watershed is flashy during the wet winter, so creek flow rates increase immediately after rainfall and then quickly fall. During the summer months, the watershed is dry, reflecting the Mediterranean-climate seasonality of the region.

The Pescadero estuary is typically highly salt stratified [*Williams*, 2014]. High freshwater inflows can flush saltwater from the system while very low summer freshwater inflow allows the lower estuary to become largely marine if the inlet remains open to the ocean. Salt dynamics in this estuary are a topic of ongoing work, but many of our efforts to characterize dynamics here are motivated by the strong stratification.

2.2. Field Measurements

Measurements were made in the lower Pescadero estuary from 17 April 2012 to 5 June 2012, with high-frequency velocity measurements limited to a shorter subset of this time. Instruments measuring velocity and pressure were distributed longitudinally in the estuary with velocity measurements at the Near Mouth (NM) and Deep Channel (DC) moorings. Pressure measurements were made at the Mid-Lagoon (ML), Pescadero Creek (PC), and Butano Creek (BC) moorings (Figure 1b).

An acoustic Doppler velocimeter (ADV; Nortek Vector) was installed on 18 April recording 512 s bursts every 15 min at a sampling rate of 8 Hz at NM (Figure 1b). The instrument's sampling volume was positioned 20 cm above the bed. A collocated conductivity, temperature, depth sensor (CTD) recorded pressure at a frequency of 1 Hz. The DC station had a bed-mounted acoustic Doppler current profiler (ADCP; RDI
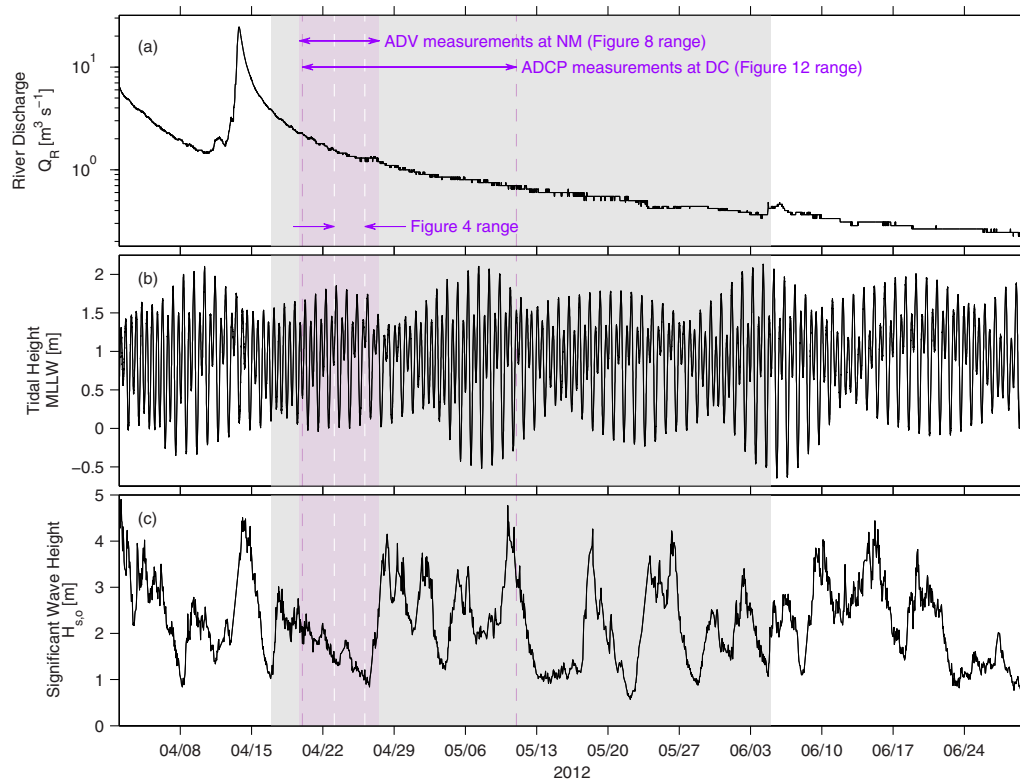
Figure 3. Conditions during field deployment. The entire data collection period is in gray with the ADV and corresponding fast-sampling CTD measurement period in purple, and ADCP measurement range indicated. (a) The freshwater streamflow into the estuary is scaled by watershed area from the USGS Pescadero gauge (11162500). (b) San Francisco tidal water level data are given by NOAA measurements at Crissy Field (9414290). (c) The NOAA NDBC buoy (46012) gives ocean significant wave height 40 km WNW of the Pescadero estuary.

Workhorse Monitor 1200 kHz). The height of the ADCP plus blanking distance meant that the first depth cell was located 71 cm above the bed at DC. In this deep region of the estuary, salt water may be trapped during neap tides [*Williams*, 2014], so the lowest ADCP measurements may show quiescent water while tidal advection acts on surface waters. The bed at DC is approximately 19 cm below MLLW. CTDs were moored upstream at PC and BC at a height of 20 cm above the bed, sampling every 30 s, but the CTD at BC only recorded for 2 weeks and is neglected in this analysis. Previous attempts to collect data in the mouth, even for a short duration (<24 h), left instruments buried in the sand, so proximity of moorings to the mouth was limited.

2.3. Data Processing

Estuarine depth measurements were made using several bed-mounted CTDs with the atmospheric pressure offset calculated from measurements made at the coastal Half Moon Bay airport (KHAF). Estuarine significant wave height, $H_{s,e}$ was calculated as $H_{s,e} = \sqrt{4m_o}$ where m_o is the variance of a 20 min moving average signal subtracted from the depth signal to remove the tidal component. Surface oscillations due to waves and bores were recorded, but infragravity oscillations considered here are of low frequency (period >30 s) so depth attenuation of the wave signal should be minimal. Some slight attenuation of the signal may occur, especially at high tide, that would result in a slight underestimation of the estuarine significant wave height.

Velocity measurements (ADV and ADCP) were rotated into principle coordinates (u, v) based on the direction of maximum variance of each instrument's data set. Tidal velocities, $\overline{u_T}$, are approximated by the depth-averaged 20 min moving average of ADCP velocity measurements. The moving average is intended to remove the higher-frequency velocity signal. The blanking distance above the bed-mounted ADCP caused the "depth-averaged" velocities to miss the bottom of the water column. While this missing data are likely relevant, the study was limited to available instruments commonly deployed in much deeper water.
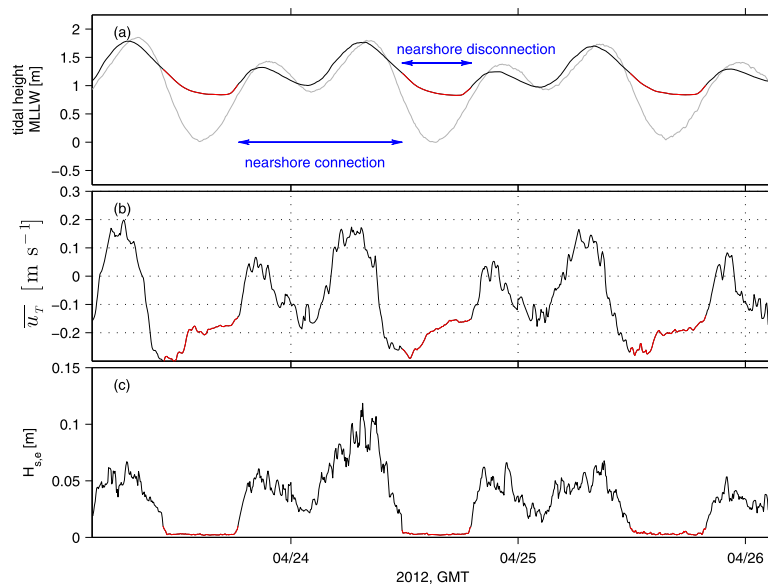
Figure 4. (a) Time series of water level, (b) depth-averaged velocity, and (c) estuarine significant wave height. Ocean water level variations (gray line) due to tides are much greater than the estuarine water level variations (black and red line). (b) Depth-averaged velocity at DC shows a sinusoidal velocity (black line) and a frictionally controlled velocity (red line) during different phases of the tide. (c) The presence of water surface oscillations is defined by an estuarine significant wave height. A threshold of 1 cm determines the presence of "waves" and (a) the water level and (b) depth-averaged velocity time series have been color coded to presence of this infragravity forcing (black—nearshore connection, red—nearshore disconnection). Scaling of $u \sim h^{1/2}$ during the frictionally controlled (red) period is shown in Figure 11.

The definition of the infragravity band varies slightly by author. Here we define the gravity wave band to be within a period of 1–30 s and the infragravity period to be from 30 s to 5 min, consistent with *Munk* [1950]. To compare tidal and infragravity kinetic energy, ADV data were low-pass filtered using a third-order Butterworth filter to remove frequencies higher than this infragravity limit. ADV tidal velocities were subsampled from a linear fit to each sampling burst. Instantaneous tidal kinetic energy was then compared to the burst average of the infragravity kinetic energy.

2.4. Overview of Conditions During Study

General conditions are based on a streamflow gauge maintained by USGS, and a tide gauge and wave buoy maintained by NOAA (Figure 3).

In California's Mediterranean climate, precipitation is seasonal and does not usually occur during the summer months. The last notable rainstorm of water year 2012 occurred between 11 and 15 April, so freshwater was present in the Pescadero estuary during the study, but no additional precipitation was recorded (Figure 3a).

The California coast experiences a mixed semidiurnal tide. The tidal range is between 1.1 and 2.7 m at the closest NOAA gauge in San Francisco (NOAA 9414290, Figures 1a and 3b). The study encompassed spring-neap variation.

A NOAA National Data Buoy Center (NDBC 46012) wave buoy in 208.8 m depth approximately 40 km WNW of the Pescadero estuary gives a proxy for the wave climate experienced at the coast (Figure 1a). Significant wave heights offshore varied between 0.6 and 4.8 m during the study (Figure 3c). The ocean wave climate changes seasonally, with maximum daily averages of up to 3 m in February and minimum daily averages of 1.4 m in August based on the 1980–2014 buoy record.

3. Tidal Time Scale Hydrodynamics and Energetics

3.1. Estuarine Tidal Elevation Behind a Shallow Inlet

Estuaries are driven by ocean tides, but lagoonal estuaries may have an attenuated tidal signal compared to the coastal ocean, usually because of friction losses [e.g., *Rydberg and Wickbom*, 1996]. By comparing water level between the ocean (Figure 4a, gray line) and the Pescadero estuary (Figure 4a, black/red line), the tidal
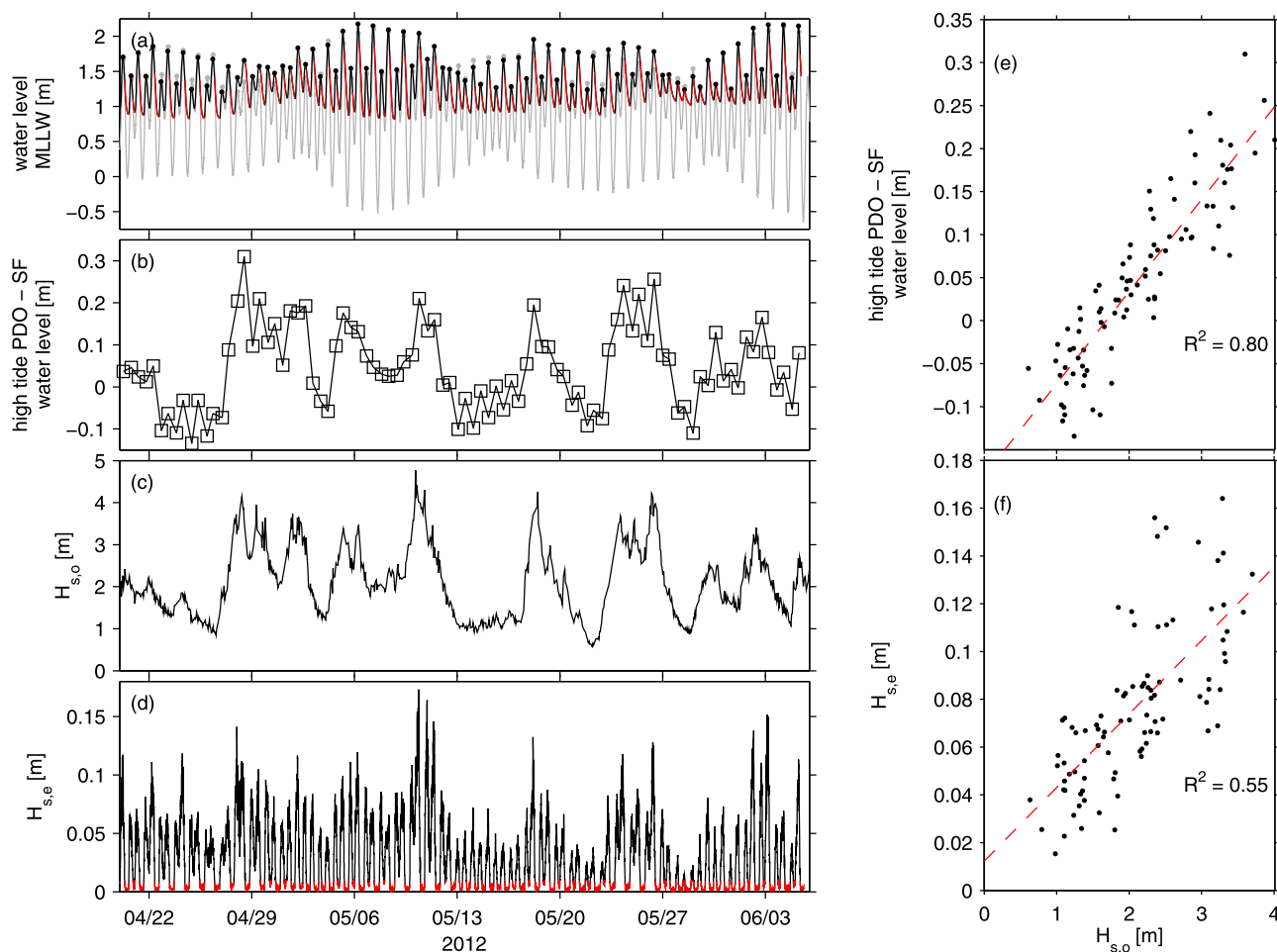
Figure 5. (a) Tidal heights in the ocean (SF) and estuary (PDO), (b) the high tide in the ocean subtracted from the corresponding high tide in the estuary, (c) significant wave height, $H_{s,o}$ in the ocean, (d) the estuarine significant wave height, $H_{s,e}$ for the study period, (e) the linear agreement between estuarine water level setup and ocean significant wave height, and (f) the relationship between the estuarine significant wave height and ocean significant wave height above the threshold of $H_{s,e} = 1$ cm. An increase of 1 m in ocean waves causes a 10 cm increase in estuarine water level setup within the Pescadero estuary. An approximate 3 cm increase in the maximum estuarine wave height occurs for every 1 m increase in ocean significant wave height.

elevations are shown to be nearly the same for most of the tidal cycle, but on the large ebb the ocean water level falls dramatically lower than the estuarine water level. Rather than a frictionally attenuated version of the ocean tide, this effect is the result of the bed of the estuarine inlet being perched above ocean low water level. The ocean water level on the three days shown retreats to below 0 m MLLW, while the estuarine water level does not fall below 0.75 m MLLW (Figure 4a).

Tidal elevation in lagoonal estuaries may also be increased when large ocean waves cause sea level setup along the coast [e.g., *Malhadas et al.*, 2009]. Subtracting the semidiurnal maximum ocean tidal elevation (in San Francisco) from the corresponding maximum estuarine water level (in the Pescadero estuary) gives the high tide estuarine water level setup (Figure 5). Linear agreement between significant wave heights in the coastal ocean and this setup shows that a 1 m increase in significant wave height causes a 0.1 m increase in tidal elevation at high tide with a linear correlation of $R^2 = 0.80$ (Figure 5e).

On this background of wave setup, ocean tides cause a varying estuarine-ocean connection. The cartoon in Figure 6 depicts the two conditions on a longitudinal section of an idealized bar-built estuary, where x is positive upstream. The height of the water column in the estuary is given by h and tidal ranges in the ocean and estuary are given by $\eta_{tide,ocean}$ and $\eta_{tide,estuary}$, respectively. The two-phase tidal cycle where the nearshore ocean and estuary are connected for 16–17 h (nearshore connection, Figure 6) and subsequently disconnected for 7–8 h (nearshore disconnection, Figure 6) of a 24 h tidal cycle sets the hydrodynamic conditions and determines different forcing depending on the height of the tide. Here we examine
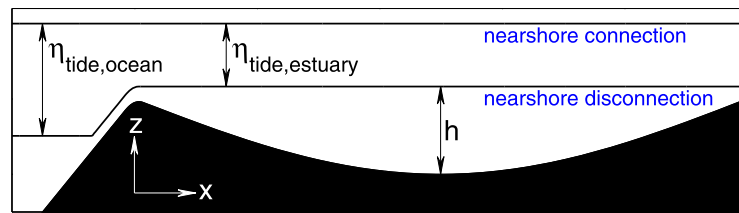
Figure 6. For most of the mixed semidiurnal tidal cycle, the estuary and ocean water levels are approximately the same, allowing for connection between the nearshore ocean and estuarine environments. As the tide falls to its daily lower low state, the ocean retreats below the mouth of the perched estuary and the nearshore ocean dynamically disconnects from the estuary.

processes during each condition and describe how the shallow inlet and tidally varying connection affects estuarine hydrodynamics.

3.2. Nearshore-Estuarine Connection

While the estuary water level and ocean water level are approximately the same, tidal velocities are sinusoidal. The tidal velocity, $\overline{u_T}$, for the small spring tide conditions on 23–26 April 2012, oscillates between -30 and $+20$ cm s^{-1} (Figure 4b, black line). Flow in the estuary is stratified with dense ocean water flooding upstream initially at depth. Later in the tide, salt water becomes trapped in deep regions (i.e., DC), and bottom waters are slow moving or quiescent while surface waters ebb [*Williams*, 2014]. This two-layer flow likely influences the apparent ebb dominance of tidal velocities shown here because missing data in the lower 71 cm of the water column should include positive flood velocities. Maximum estuarine water level leads peak flood tidal velocities by 1–2 h (Figures 4a and 4b).

3.2.1. Presence of Infragravity Forcing

On top of the tidally induced velocities and changes in water level, oscillating motions are observed during the nearshore-estuarine connection phase of the tide in both velocity and as a surface expression. Figure 7
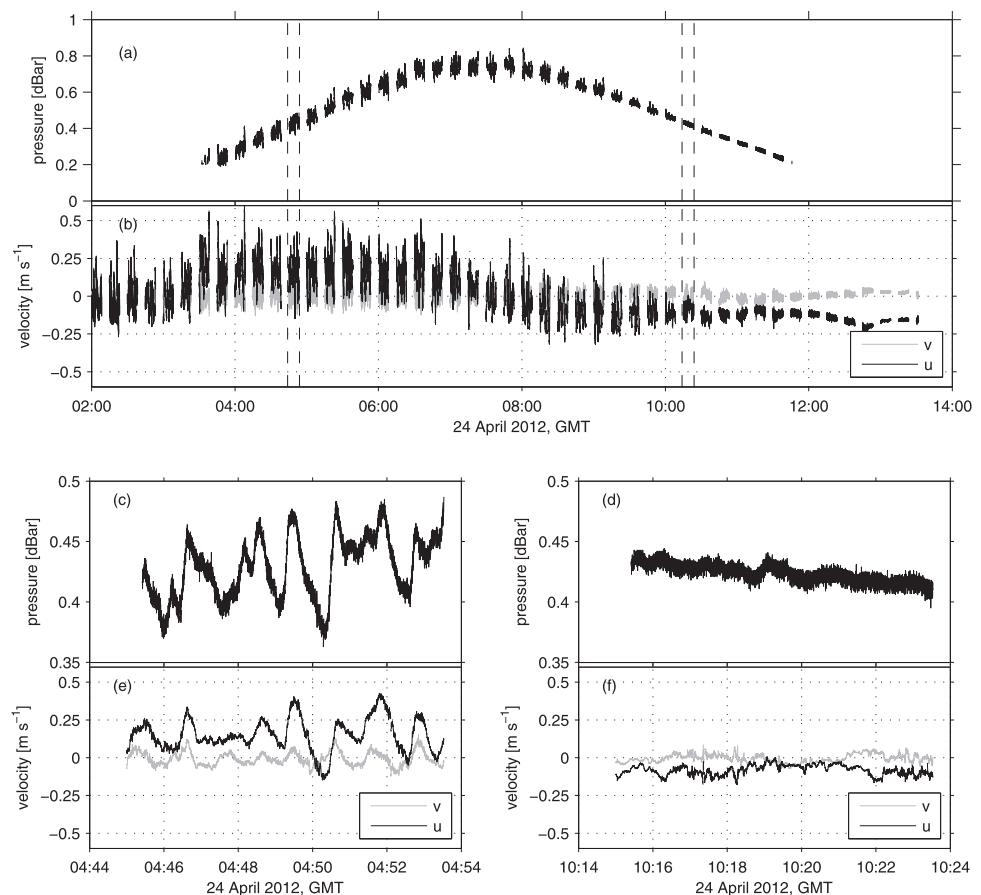

Figure 7. (a) The pressure record and (b) *u* and *v* components of velocity from an ADV measuring 20 cm above the bed at the NM station. (c–f) The remaining plots show two bursts (denoted by dashed lines in Figures 7a and 7b) when the tide was (c, e) flooding and (d, f) ebbing at the same water depth. During flood large velocity oscillations occur with the surface motions. On ebb, these wave-like oscillations are cut off in both pressure and velocity. The first 25 s of each pressure burst has been removed due to apparent aliasing.
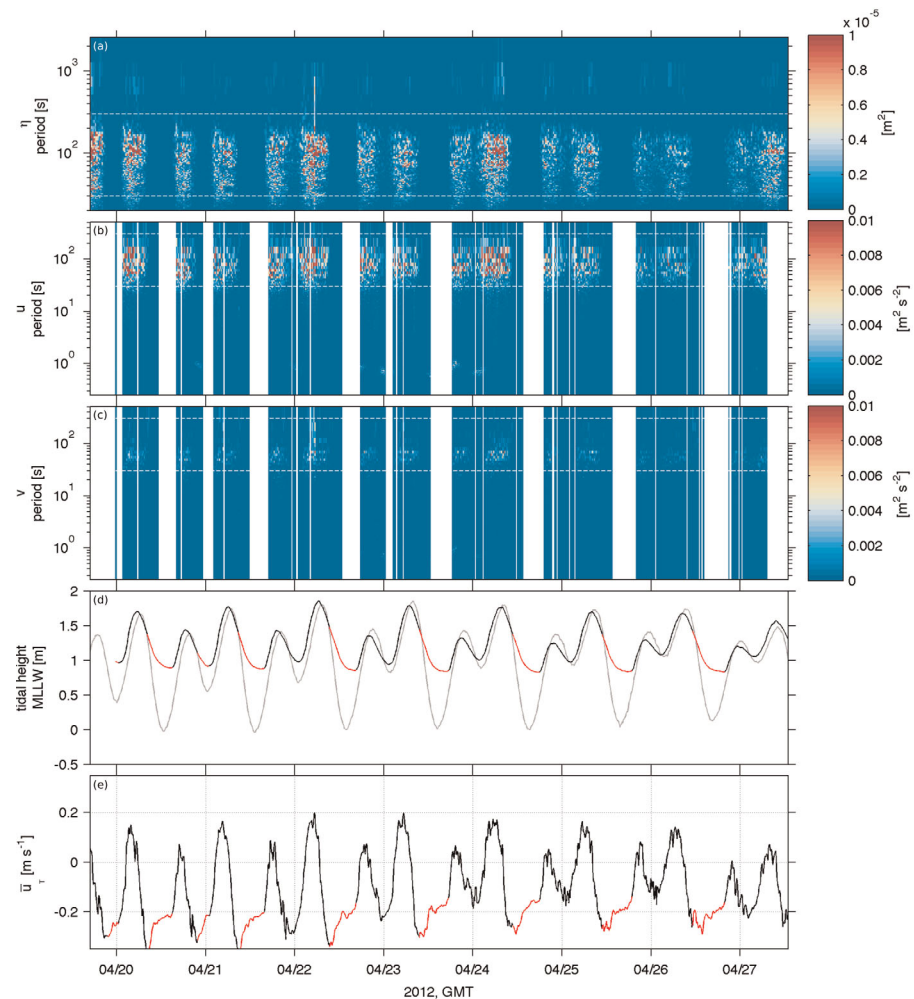
Figure 8. (a) Variance preserving spectra of depth (1 Hz CTD measurement), (b) velocity u, and (c) velocity v (8 Hz ADV measurements). Where data exist, spectra are computed on each burst. The white dashed lines indicate the infragravity period limits of 30–300 s. The CTD measuring pressure was always submerged but the ADV came out of the water at some low tides, causing data dropouts. (d) The tidal height in Pescadero and at San Francisco, and (e) the depth-averaged tidal velocities in Pescadero corresponding show the tidal dependence of infragravity forcing.

shows pressure and velocity from an ADV at NM. Over the course of a flood and ebb tide, large oscillations in (a) pressure and (b) velocity are observed on short time scales. These oscillations are present on the rising tide (Figures 7c and 7e), but on the ebb corresponding to the same water level the oscillations cease (Figures 7d and 7f).

The oscillations in pressure and velocity are attributed to the presence of infragravity motions in the nearshore because their observed period is within the infragravity band of 30 s to 5 min (Figure 8). Infragravity waves can be locally generated as shorter period wind waves interact with each other and the coast, or can be generated remotely and propagate across the ocean [*Herbers et al.*, 1995; *Holman*, 1981]. These waves are observed in all parts of the ocean, but are largest at the coast [*Webb et al.*, 1991; *Longuet-Higgins and Stewart*, 1962; *Elgar et al.*, 1992]. No instrumentation was deployed in the nearshore during this field campaign, but infragravity motions are consistently present on sandy beaches and are expected to be present here [*Contardo and Symonds*, 2013]. Characterizing the surface oscillations as an estuarine significant wave height, $H_{s,e}$ (Figure 4c) gives a metric for the presence of infragravity motions in the estuary and thus a proxy for nearshore-estuarine connection. When $H_{s,e}$ is greater than 1 cm (Figure 4, black lines), the relationship between ocean tides and estuarine tides are nearly 1:1, and tidal velocities obey an expected sinusoidal shape in relation to tidal water level. A value of $H_{s,e}$ below 1 cm indicates that the ocean infragravity
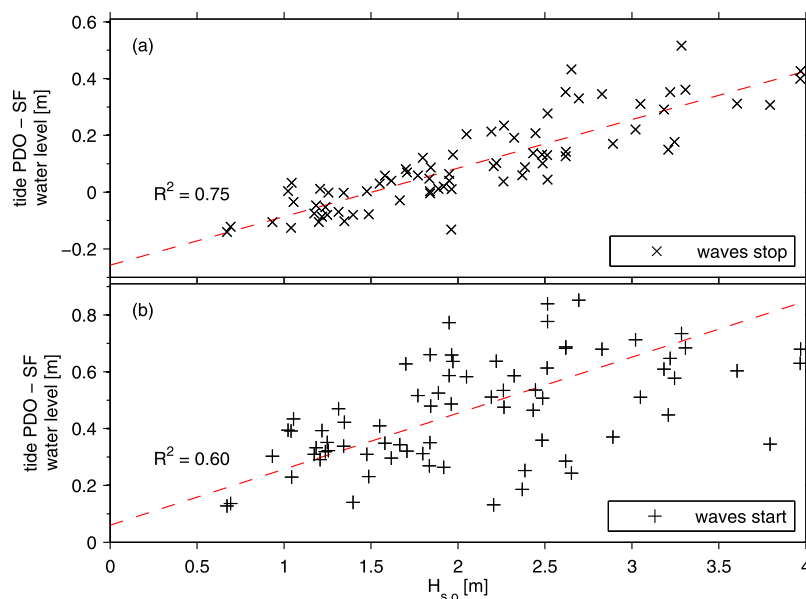
Figure 9. The difference between estuarine and ocean water level at the moment of (a) dynamic disconnection (wave shutoff) and (b) reconnection of the nearshore ocean to the estuary is modulated by the ocean wave climate. The slopes of the linear fits are (a) 17 cm m^{-1} and (b) 20 cm m^{-1}.

motions are no longer reaching the estuary and thus communication between the nearshore and estuary has ceased (Figures 4a and 4c, red lines).

The dynamic disconnection of the estuary and nearshore ocean occurs when the ocean retreats to some point below the mouth of the estuary. Plotting the difference between water level measurements in the Pescadero estuary and in the ocean at the moments of dynamic disconnection and reconnection shows wave setup of the nearshore ocean again influences connectivity (Figure 9). The disparity between the estuarine and oceanic water levels is a function of ocean significant wave height ($R^2 = 0.75$ for wave stoppage and $R^2 = 0.60$ for the resumption of infragravity motions), suggesting that disconnection occurs at a relatively constant differential between the estuarine and nearshore ocean water level, but this elevation is not captured by a tide gauge outside of the surf zone. Unlike high tide water level setup measurements (Figure 5e), the data in Figure 9 do not account for timing differences as the tidal wave propagates northward. This bias will cause an underestimation of the water level differential on wave shutoff and an overestimation on wave startup.

Hydraulic control at the inlet could provide an alternate explanation for wave shutoff with a critical or supercritical Froude number ($Fr = \frac{u}{\sqrt{gH}} \geq 1$). Data showed the Froude number at the moment of wave shutoff to track velocity, varying with the spring-neap cycle. Lack of constancy of the Froude number at shutoff leads us to discount the possibility of wave blocking by hydraulic control in the Pescadero inlet.

3.2.2. Infragravity Velocity Oscillations

Infragravity motions induce high-velocity oscillations in the estuary. On an incoming tide, infragravity motions in the nearshore cause bores to propagate into and up the estuary. We believe the bores are formed by waves and swash being funneled and accelerated up the narrow inlet (Figure 2), inducing rapid flow and a propagating hydraulic jump, similar to the formation of tidal bores. Run-up of swash in the infragravity band increases with ocean significant wave height [e.g., *Guza and Thornton*, 1982] and is consistent with the increase of estuarine wave height induced by this nearshore forcing (Figure 5f).

The infragravity motion-induced bores resemble tidal bores seen in some shallow estuaries on coasts with large tidal ranges. Field observations of tidal bores show that undular tidal bores do little to dissipate tidal energy [*Wolanski et al.*, 2004] while breaking tidal bores contribute an energetic burst of turbulent kinetic energy [*Simpson et al.*, 2004]. The bore structure in the Pescadero estuary as the tide rises is usually undular but has been visually observed to be breaking when ocean waves are very large.

In phase with these bores are velocity oscillations larger than the tidal velocities (Figures 7c and 7e). The stacked variance preserving spectra shows little energy in the gravity wave band (period 1–30 s, Figure 8).

These data agree with visual observations that ocean gravity waves break on the beach outside the estuarine mouth. In this way, the beach and inlet act as a low-pass filter to remove the higher-frequency waves. Lower-frequency infragravity energy passes through the mouth. In the small Pescadero estuary, infragravity surface motions were observed at all moorings, and the corresponding velocity signature was present at all locations where velocity was measured. Surface expressions of infragravity motions appear to propagate upstream only. Higher-frequency infragravity motions may be damped in the lower estuary with lower frequencies propagating further upstream (data not shown). Early in the flood tide while these motions are seen as bores, they break or are absorbed by the periphery of the estuary. As the tide rises, these motions are less visible to the eye, and probably dissipate in the channelized marsh periphery. Were the Pescadero estuary a harbor or basin with a solid upstream wall, resonance or a seiche induced by infragravity motions would likely occur [e.g., *Thotagamuwage and Pattiaratchi*, 2014].

Spectral analysis further illustrates the activation and disconnection of the nearshore influence (Figure 8). Plotted with variance preserving spectra of (a) pressure and (b, c) velocity are the (d) water level and (e) tidally averaged velocity. The strength of the infragravity signal varies with the oceanic wave climate. Larger waves in the ocean also correspond with larger waves within the estuary. As the ocean significant wave height increases, so does the tidally modulated estuarine significant wave height (Figures 5b and 5d). Comparing peak $H_{s,e}$ values to the ocean significant wave height $H_{s,o}$, we see a 1 m increase in ocean waves increases the maximum estuarine significant wave height by 3 cm. A linear correlation gives a value of $R^2 = 0.55$. Wave interaction with the beach, inlet, estuary, and tidal currents is expected to induce nonlinearities, so this linear correlation is not expected to be very high.

3.2.3. Energetics of Infragravity Motions

Considering the kinetic energy per unit volume in the water column,

$$KE = \frac{1}{2}\rho(u^2 + v^2),$$ (1)

infragravity motions are a relevant component of overall estuarine energetics. Measurements of tidal and infragravity u and v velocities are shown for one tidal cycle on 23–24 April 2012 with kinetic energy calculated from the horizontal components of velocity (Figure 10). The oscillatory infragravity signal varies through the tidal cycle: maximum oscillations occur with the highest flood velocities (20:00–00:00 on 23 April), oscillations are damped during the small ebb (15:00–19:00 on 23 April), and then oscillatory flow stops (05:00 on 24 April, Figures 10a and 10b). Figure 10c shows that both the tidal (low frequency) and infragravity components of kinetic energy vary tidally, as do their overall contribution to the energetics. Strong flood tides are accompanied by large infragravity oscillations which are about 20% of the combined kinetic energy. At slack tide the infragravity signal remains, becoming 100% of the kinetic energy in the system. During the large ebb, the infragravity motions are cut off and the opposite is true.

Infragravity motions move the entire water column back and forth, similar to a very short tide. Interaction of this oscillating water column with boundaries, bathymetric features, or vegetation can induce shear in the water column as a boundary layer forms and lead to scalar mixing. In small, salt-stratified estuaries, like Pescadero, infragravity motions are observed throughout the estuary and may be important to salinity transport and mixing [*Williams*, 2014]. Work to quantify salinity dispersion in the Pescadero estuary is ongoing. In the functionally similar but larger Russian River estuary [*Behrens*, 2012], high energy events may contribute to buoyancy mixing near the mouth, thus influencing the salinity of ocean-sourced water being advected upstream to where other processes may dominate mixing and transport. In largely marine systems such as the Albufeira lagoon in Portugal where freshwater inflow is low [*Dodet et al.*, 2013], high velocities near the mouth will still contribute to mixing, but with no discernible density stratification influence will be limited to other scalars.

Infragravity motions are seen to be relevant for sediment transport in the surf zone, tidal inlets, and in the closed state of intermittently closed estuaries, swash overwash is the mechanism by which the sand berm grows [*Beach and Sternberg*, 1988; *Green and MacDonald*, 2001; *Baldock et al.*, 2008]. In the Pescadero estuary where in the open state the magnitude of velocities attributed to infragravity motions are similar or larger than the tidal velocity, we expect this flow to be responsible for resuspending sediment and dominant in geomorphological change. While the mouth of the Pescadero estuary is closed, swash overwash is observed to occur on infragravity time scales. This overwash has been seen to raise the water level of the
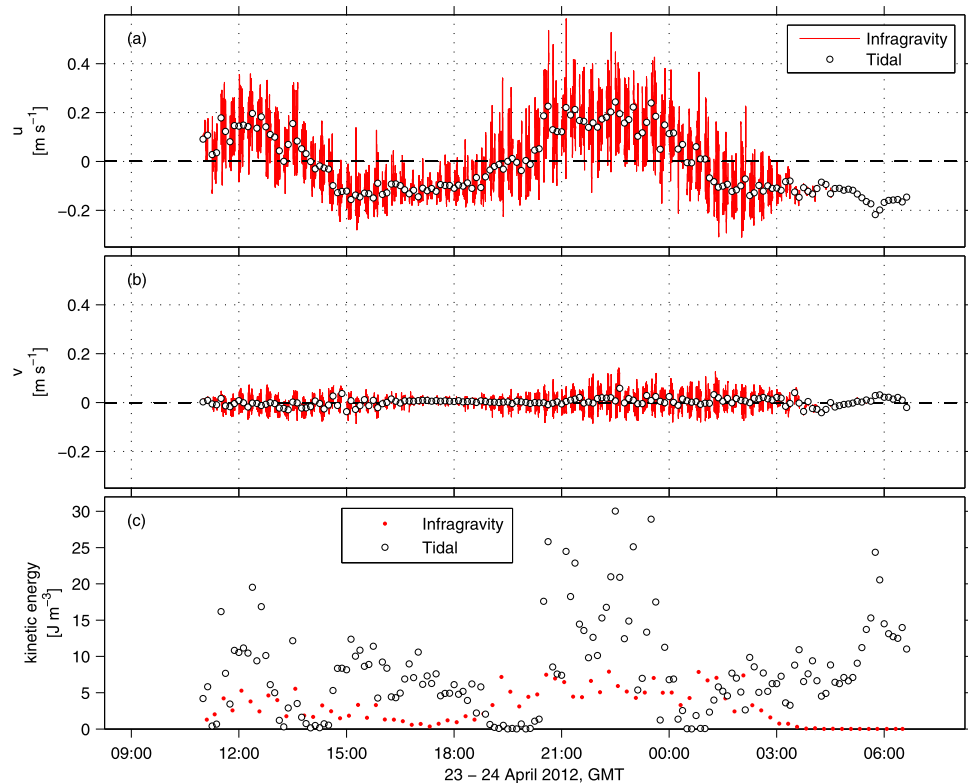
Figure 10. Velocity and kinetic energy measurements by the ADV at NM. (a) The u component of velocity, (b) the v component of velocity, and (c) the kinetic energy calculated using the horizontal components of velocity.

closed lagoon (data not shown) and must be accompanied by geomorphic change as seen in the accretion of sediments at the mouth of this and other estuaries [*Baldock et al.*, 2008].

The presence of infragravity waves in sandy inlets has been previously observed [*Schubert and Bokuniewicz*, 1991], but recently has received renewed attention. Currents up to 40 cm s^{-1} in the Ría de Santiuste in Northern Spain oscillate on infragravity time scales [*Uncles et al.*, 2014]. Work focused on wave-current interaction in the inlet to the Portuguese Albufeira lagoon noted the presence of velocities on an infragravity time scale equal to 50% of the tidal velocities [*Dodet et al.*, 2013]. Elsewhere in California, surface oscillations on an infragravity time scale were observed in the Russian River estuary at a measurement location 2.4 km from the mouth for the two days between the closed inlet opening to the reclosure in early October 2010 while observations 7.4 km from the mouth did not exhibit these oscillations (data not shown). Similar to the tidally discontinuous forcing in the Pescadero estuary, surface oscillations ceased for part of the tidal cycle. The dominant infragravity frequencies were lower in the Russian River estuary than in the Pescadero estuary, probably because the higher frequencies dissipate closer to the mouth as seen in the Pescadero estuary and inferred by the lack of an infragravity signal 7.4 km from the mouth of the Russian River. Given the expected presence of infragravity motions on beaches worldwide [*Contardo and Symonds*, 2013] and given the observed presence of an infragravity signal in sandy inlets and bar-built estuaries, we conclude that this forcing is likely ubiquitous in estuaries with very shallow, sandy inlets.

3.3. Nearshore-Estuarine Disconnection and Frictional Control

As the ocean water level falls with the outgoing tide, the estuarine water level also drops, but at a much slower rate (Figure 4a). During this period, the estuary becomes dynamically disconnected from the influence of the nearshore ocean. The depth-averaged tidal velocity is no longer sinusoidal, but has a maximum ebb velocity as the infragravity motions are stopping (Figures 4b and 8e).

On tidal flats at low tide, a frictional control is observed [e.g., *Ralston et al.*, 2013]. In our case, the shape of the velocity curve, the change in the rate of estuarine water level fall, and the water surface elevation disparity between the ocean and estuary all suggest that the draining estuary reaches a frictionally controlled
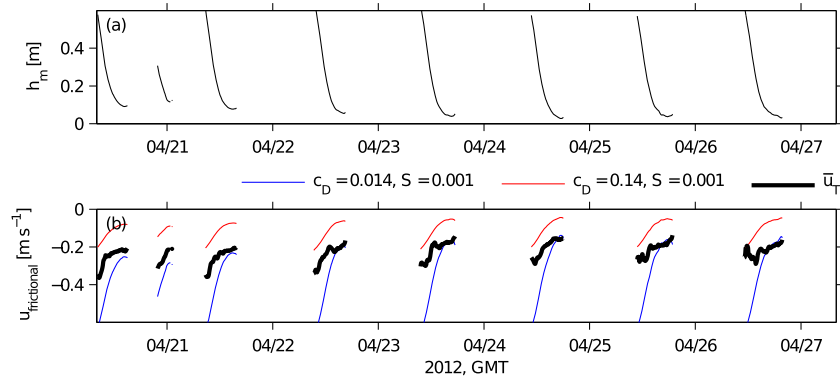
Figure 11. (a) Approximate water level height at the mouth, h_m and (b) resulting velocity in a frictionally controlled state given approximate values of c_D and S. The depth-averaged tidal velocity measured at DC is plotted in black for comparison.

state. An analytical description of frictionally controlled velocity is reached starting with the incompressible Reynolds-averaged Navier-Stokes (RANS) equations:

$$\frac{\partial u_i}{\partial t} + u_j \frac{\partial u_i}{\partial x_j} = -\frac{1}{\rho_0}\frac{\partial p}{\partial x_i} + \frac{\partial}{\partial x_j}\left(v_T \frac{\partial u_i}{\partial x_j}\right) - g\delta_{i3}$$

$$\frac{\partial u_i}{\partial x_i} = 0. \tag{2}$$

The x momentum RANS equation along a bed of slope angle θ is

$$\frac{\partial u}{\partial t} + u\frac{\partial u}{\partial x} + v\frac{\partial u}{\partial y} + w\frac{\partial u}{\partial z} =$$

$$-\frac{1}{\rho_0}\frac{\partial p}{\partial x} + \frac{\partial}{\partial x}\left(v_T \frac{\partial u}{\partial x}\right) + \frac{\partial}{\partial y}\left(v_T \frac{\partial u}{\partial y}\right) + \frac{\partial}{\partial z}\left(v_T \frac{\partial u}{\partial z}\right) + g\sin\theta, \tag{3}$$

where v_T is the turbulent viscosity and θ is the angle of the bed slope. In a frictionally controlled state, the flow is fully developed, steady state, two-dimensional, and the water surface slope is the same as the bed slope. Under these assumptions, equation (3) reduces to:

$$0 = \frac{\partial}{\partial z}\left(v_T \frac{\partial u}{\partial z}\right) + g\sin\theta. \tag{4}$$

Depth-averaging ($\bar{u} = \frac{1}{h}\int_0^h u\,dz$) equation (4) with bed stress ($v_T \frac{\partial u}{\partial z}|_{z=0} = \frac{\tau_b}{\rho}$) and free-surface ($v_T \frac{\partial u}{\partial z}|_{z=h} = 0$) boundary conditions where τ_b is bed stress and z is positive upward from the bed gives

$$0 = -\frac{\tau_b}{h\rho} + g\sin\theta. \tag{5}$$

Using a friction velocity (u_*) parameterization, $\tau_b = \rho u_*^2$, $u_*^2 = c_D \bar{u}^2$, and the small-angle approximation of $\sin\theta \sim S$, where c_D is a bed drag coefficient that accounts for roughness due to bed material and bed forms, S is the bed slope, $\bar{u}$ is a depth-averaged velocity gives

$$c_D \bar{u}^2 = gSh. \tag{6}$$

Given relatively constant values of S and c_D, the depth-averaged velocity $\bar{u} \sim h^{\frac{1}{2}}$. This describes the shape of the velocity curve during this frictionally controlled state (Figures 4b and 11).

Although survey data for the actual slope of the mouth is unavailable, using reasonable estimates we can constrain the coefficient of drag, c_D that is required dynamically by equation (6). Assuming the water surface slope matches the bed slope at the mouth and is flat across the lower estuary and no hydraulic jumps occur between the central estuary and the mouth, by conservation of mass at the mouth (subscript m) and DC station (subscript DC),

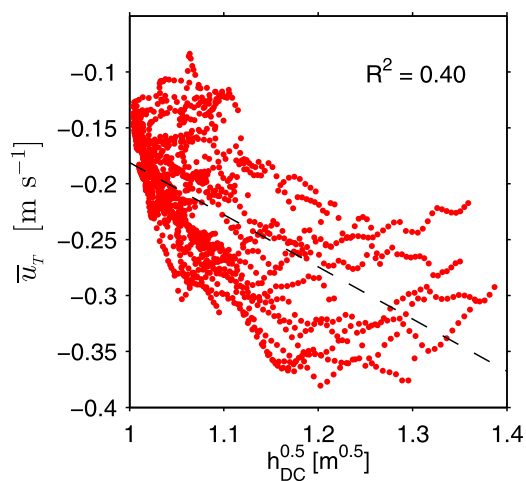$$\bar{u}_m = \frac{\bar{u}_{DC} A_{DC}}{A_m}, \tag{7}$$

Figure 12. Depth and velocity data are plotted against each other for the spring tides shown in Figure 13. Measurements from 28 April to 4 May are excluded because data dropouts and unmoving bottom water at DC influence the depth-averaged velocity.

where A_m is cross-sectional area of the channel and A_{DC} is the cross-sectional area at station DC (each estimated from bathymetry measurements at the site).

For a range of possible bed slopes (S between 0.001 and 0.01, say) and for characteristic early frictional control values of $\bar{u}_{DC} = -0.3$ m s^{-1} and $h_{DC} = 1.45$ m, we constrain the drag coefficients to be between 0.014 and 0.14. Characteristic late frictional control values of $\bar{u}_{DC} = -0.2$ m s^{-1} and $h_{DC} = 1$ m give a range of c_D from 0.002 to 0.02. Plotted in Figure 11 are approximations of h_m and the corresponding frictionally controlled velocity, u with some values of c_D and S under the assumptions made here.

A typical value for c_D of a sandy bed is 0.004 [*Soulsby*, 1983] and this value has been observationally recorded in inlets to tidal lagoons [*Rydberg and Wickbom*, 1996]. Bed forms at the mouth of the Pescadero estuary would be expected to increase the drag above $c_D = 0.004$, but do not probably account for the very high drag suggested early in the ebb. It is not surprising that the early ebb has a bias in this estimate, due to the evolving nature of the water surface profile; it is much more likely that the frictional control approximation will be accurate later in the ebb tide.

In the end, the key factor motivating the use of a frictional control framework is the overall shape of the velocity profile, which is consistent with $\bar{u} \sim h^{\frac{1}{2}}$; simply plotting u with $h^{\frac{1}{2}}$ for the tidally disconnected state shows a nonlinear process (Figure 12). It should be noted that in contrast to the limited tidal range caused by the shallow inlet in the Pescadero estuary, bed friction coupled with Bernoulli acceleration explains
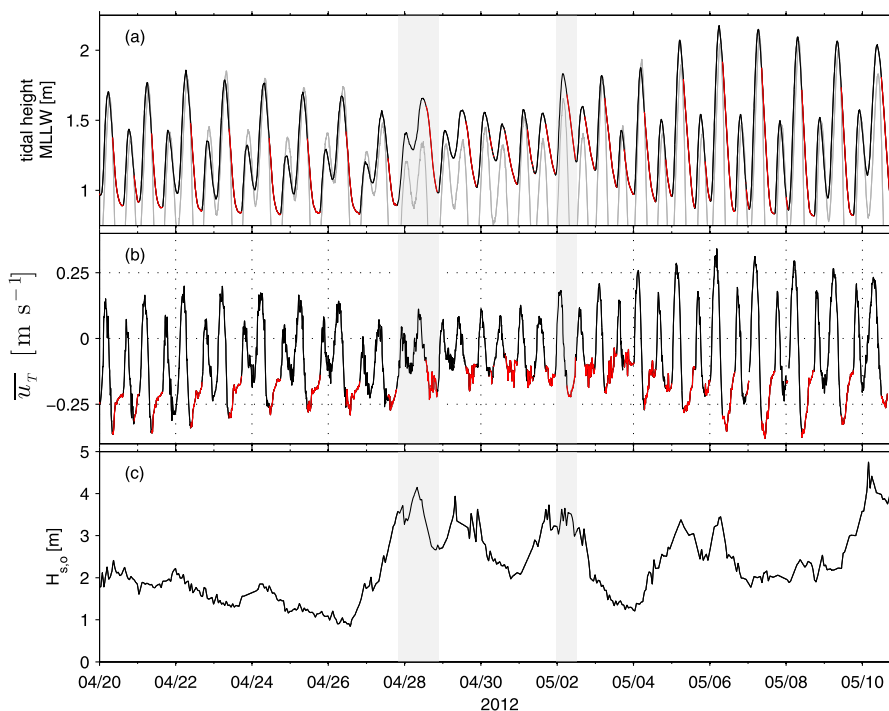

Figure 13. (a) The longer time series of estuarine water level (black/red) and ocean water level (gray), (b) depth-averaged tidal velocities, and (c) ocean significant wave height show that the general trend of oscillation between ocean/wave forced (black lines) and nonwavy (red lines) persists through the spring-neap cycle. Periods in gray are discussed in section 4.

water level differences between the ocean and lagoon in other tidally choked systems [e.g., *Rydberg and Wickbom*, 1996; *Hill*, 1994] based on the formulation $|h_o - h_i| = \left(1 + \frac{C_D BL}{A}\right)\frac{u^2}{2g}$ [*Stigebrandt*, 1980]. This formulation expects water surface slope in the inlet to be independent of the bed slope, a condition not observed in the Pescadero estuary on the large ebb. Furthermore, in the Pescadero estuary, a very short channel between the ocean and the estuary limits the frictional effects on the rising tide and slow velocities make the Bernoulli acceleration term very small.

4. Variability on Longer Time Scales

While the inlet of the Pescadero estuary is open, the previously described tidally varying processes occur. The spring-neap tidal cycle modulates the tidal velocity (Figures 13a and 13b). Wave shut off occurs consistently on the large ebb of the semidiurnal spring or neap tide (Figure 13, red lines). The shape of the depth-averaged velocity with time is consistent with our understanding of frictional control for spring tide conditions (Figures 13b and 13d). During the neap tide, the frictionally dominated velocity-water level relationship of $\bar{u} \sim h^{\frac{1}{2}}$ is not clear. Characteristic of this and other small bar-built estuaries, salt water may become trapped in deep regions for several tidal cycles during the neap tide [*Blanton et al.*, 2000; *Williams*, 2014]. During this time, the ADCP, located in the deep region of the lower Pescadero estuary, sampled the trapped bottom water and the moving surface waters. Measurement dropouts were frequent. The slow or still lower water column measurements dominate the depth-averaged velocity. The characteristic frictionally controlled velocity shape appears to be present in the surface measurements during these periods, but data are sparse thus not presented here. Work to characterize the salinity dynamics of this estuary is on-going.

The spring-neap cycle may also be altered by a large ocean wave climate. The tidal water level on 28 April is distorted in alignment with ocean significant wave heights of 4 m (Figures 13a and 13c, indicated by gray bars). Here the tidal signal was transitioning into a neap, so velocities and water level should have been decreasing, but water level increased and the tidal velocity was roughly the same as the previous day. A bigger jump in wave setup on 2 May corresponded with an increase in velocities. In general, higher flood velocities occur with higher water levels whether the higher water level is attributed to the spring tides or wave setup. These features are simply a function of conservation of mass, but again indicate that understanding ocean tidal conditions is insufficient to explain tidal water levels and velocities in small bar-built estuaries.

5. Conclusions

We have observed dominant hydrodynamic processes within one California estuary which are likely similar to those present in similar estuaries along the western coast of the Americas as well as in Australia, South Africa, and in estuaries in Mediterranean climates on the Atlantic west coast of Europe, as well as in shallow sandy inlets elsewhere.

We see that in the open state of intermittently open estuaries:

1. The mouth of the estuary may remain perched above low water in the ocean, and wave setup as well as tides set the estuarine water level.
2. The perched mouth limits tidal velocities and does not allow ocean gravity waves to enter the estuary but permits infragravity motions to pass through the inlet.
3. High velocities induced by these infragravity motions are energetically important.
4. On the large ebb, the ocean retreats from the mouth, nearshore forcing is cut off, and frictional control describes the velocity.

This work has highlighted the strong dependence of hydrodynamics of small bar-built estuaries on nearshore processes. Future field observations in these estuaries should include nearshore measurements to better quantify this connection.

References

Baldock, T. E., F. Weir, and M. G. Hughes (2008), Morphodynamic evolution of a coastal lagoon entrance during swash overwash, *Geomorphology*, 95(3–4), 398–411, doi:10.1016/j.geomorph.2007.07.001.

Battjes, J. A. (1988), Surf-zone dynamics, *Annu. Rev. Fluid Mech.*, 20(1), 257–291, doi:10.1146/annurev.fl.20.010188.001353.

Beach, R. A., and R. W. Sternberg (1988), Suspended sediment transport in the surf zone: Response to cross-shore infragravity motion, *Mar. Geol.*, *80*(1–2), 61–79, doi:10.1016/0025-3227(88)90072-2.

Becker, J. M., M. A. Merrifield, and M. Ford (2014), Water level effects on breaking wave setup for Pacific Island fringing reefs, *J. Geophys. Res. Oceans*, *119*, 914–932, doi:10.1002/2013JC009373.

Behrens, D. K. (2012), The Russian River estuary: Inlet morphology, management, and estuarine scalar field response, PhD thesis, Univ. of Calif., Davis, Calif.

Behrens, D. K., F. A. Bombardelli, J. L. Largier, and E. Twohy (2013), Episodic closure of the tidal inlet at the mouth of the Russian River—A small bar-built estuary in California, *Geomorphology*, *189*, 66–80, doi:10.1016/j.geomorph.2013.01.017.

Blanton, J. O., M. A. Ferreira, and F. A. Andrade (2000), Effect of a broad shallow sill on tidal circulation and salt transport in the entrance to a coastal plain estuary (Mira-Vila Nova de Milfontes, Portugal), *Estuaries*, *23*(3), 293–304, doi:10.2307/1353322.

Clarke, D. W., J. F. Boyle, R. C. Chiverrell, J. Lario, and A. J. Plater (2014), A sediment record of barrier estuary behaviour at the mesoscale: Interpreting high-resolution particle size analysis, *Geomorphology*, *221*, 51–68, doi:10.1016/j.geomorph.2014.05.029.

Contardo, S., and G. Symonds (2013), Infragravity response to variable wave forcing in the nearshore, *J. Geophys. Res. Oceans*, *118*, 7095–7106, doi:10.1002/2013JC009430.

Dodet, G., X. Bertin, N. Bruneau, A. B. Fortunato, A. Nahon, and A. Roland (2013), Wave-current interactions in a wave-dominated tidal inlet, *J. Geophys. Res. Oceans*, *118*, 1587–1605, doi:10.1002/jgrc.20146.

Elgar, S., T. H. C. Herbers, M. Okihiro, J. Oltman-Shay, and R. T. Guza (1992), Observations of infragravity waves, *J. Geophys. Res.*, *97*(C10), 15,573–15,577, doi:10.1029/92JC01316.

Elwany, M. H. S., R. E. Flick, and S. Aijaz (1998), Opening and closure of a marginal Southern California lagoon inlet, *Estuaries*, *21*(2), 246–254.

Fortunato, A. B., et al. (2014), Morphological evolution of an ephemeral tidal inlet from opening to closure: The Albufeira inlet, Portugal, *Cont. Shelf Res.*, *73*, 49–63, doi:10.1016/j.csr.2013.11.005.

Gale, E., C. Pattiaratchi, and R. Ranasinghe (2007), Processes driving circulation, exchange and flushing within intermittently closing and opening lakes and lagoons, *Mar. Freshwater Res.*, *58*(8), 709–719, doi:10.1071/MF06121.

Green, M. O., and I. T. MacDonald (2001), Processes driving estuary infilling by marine sands on an embayed coast, *Mar. Geol.*, *178*(1–4), 11–37, doi:10.1016/S0025-3227(01)00188-8.

Guza, R. T., and E. B. Thornton (1982), Swash oscillations on a natural beach, *J. Geophys. Res.*, *87*(C1), 483–491, doi:10.1029/JC087iC01p00483.

Hanes, D. M., K. Ward, and L. H. Erikson (2011), Waves and tides responsible for the intermittent closure of the entrance of a small, sheltered tidal wetland at San Francisco, CA, *Cont. Shelf Res.*, *31*(16), 1682–1687, doi:10.1016/j.csr.2011.07.004.

Herbers, T. H. C., S. Elgar, and R. T. Guza (1995), Generation and propagation of infragravity waves, *J. Geophys. Res.*, *100*(C12), 24,863–24,872, doi:10.1029/95JC02680.

Hill, A. E. (1994), Fortnightly tides in a lagoon with variable choking, *Estuarine Coastal Shelf Sci.*, *38*(4), 423–434, doi:10.1006/ecss.1994.1029.

Holman, R. A. (1981), Infragravity energy in the surf zone, *J. Geophys. Res.*, *86*(C7), 6442–6450, doi:10.1029/JC086iC07p06442.

Largier, J. L., and S. Taljaard (1991), The dynamics of tidal intrusion, retention, and removal of seawater in a bar-built estuary, *Estuarine Coastal Shelf Sci.*, *33*(4), 325–338.

Longuet-Higgins, M. S., and R. W. Stewart (1962), Radiation stress and mass transport in gravity waves, with application to 'surf beats,' *J. Fluid Mech.*, *13*(4), 481–504, doi:10.1017/S0022112062000877.

Malhadas, M. S., P. C. Leitão, A. Silva, and R. Neves (2009), Effect of coastal waves on sea level in Óbidos Lagoon, Portugal, *Cont. Shelf Res.*, *29*(9), 1240–1250, doi:10.1016/j.csr.2009.02.007.

Mei, C. C., and P. L. Liu (1993), Surface waves and coastal dynamics, *Annu. Rev. Fluid Mech.*, *25*(1), 215–240, doi:10.1146/annurev.fl.25.010193.001243.

Monismith, S. G. (2007), Hydrodynamics of coral reefs, *Annu. Rev. Fluid Mech.*, *39*(1), 37–55, doi:10.1146/annurev.fluid.38.050304.092125.

Munk, W. H. (1950), Origin and generation of waves, *Coastal Eng. Proc.*, *1*(1), 1, doi:10.9753/icce.v1.1.

Nwogu, O., and Z. Bemirbilek (2010), Infragravity wave motions and runup over shallow fringing reefs, *J. Waterw. Port Coastal Ocean Eng.*, *136*(6), 295–305, doi:10.1061/(ASCE)WW.1943-5460.0000050.

Ralston, D. K., W. R. Geyer, P. A. Traykovski, and N. J. Nidzieko (2013), Effects of estuarine and fluvial processes on sediment transport over deltaic tidal flats, *Cont. Shelf Res.*, *60*, S40–S57, doi:10.1016/j.csr.2012.02.004.

Ranasinghe, R., and C. Pattiaratchi (1999), Circulation and mixing characteristics of a seasonally open tidal inlet: A field study, *Mar. Freshwater Res.*, *50*(4), 281–290.

Ranasinghe, R., and C. Pattiaratchi (2003), The seasonal closure of tidal inlets: Causes and effects, *Coastal Eng. J.*, *45*(4), 601–627, doi:10.1142/S0578563403000919.

Rich, A., and E. A. Keller (2013), A hydrologic and geomorphic model of estuary breaching and closure, *Geomorphology*, *191*, 64–74, doi:10.1016/j.geomorph.2013.03.003.

Rydberg, L., and L. Wickbom (1996), Tidal choking and bed friction in Negombo Lagoon, Sri Lanka, *Estuaries*, *19*(3), 540–547, doi:10.2307/1352516.

Schubert, C. E., and H. J. Bokuniewicz (1991), Infragravity wave motion in a tidal inlet, in *Coastal Sediments '91: Proceedings of a Specialty Conference on Quantitative Approaches to Coastal Processes: Seattle, Washington*, vol. 2, edited by N. C. Kraus, K. J. Gingerich, and D. L. Kriebel, pp. 1434–1446, Am. Soc. of Civ. Eng., Seattle, Wash.

Simpson, J. H., N. R. Fisher, and P. Wiles (2004), Reynolds stress and TKE production in an estuary with a tidal bore, *Estuarine Coastal Shelf Sci.*, *60*(4), 619–627, doi:10.1016/j.ecss.2004.03.006.

Soulsby, R. L. (1983), The bottom boundary layer of shelf seas, in *Physical Oceanography of Coastal and Shelf Seas*, vol. 35, edited by B. Johns, pp. 189–266, Elsevier, Amsterdam.

Stigebrandt, A. (1980), Some aspects of tidal interaction with fjord constrictions, *Estuarine Coastal Mar. Sci.*, *11*(2), 151–166, doi:10.1016/S0302-3524(80)80038-7.

Thotagamuwage, D. T., and C. B. Pattiaratchi (2014), Observations of infragravity period oscillations in a small marina, *Ocean Eng.*, *88*, 435–445, doi:10.1016/j.oceaneng.2014.07.003.

Uncles, R. J., J. A. Stephens, and C. Harris (2014), Infragravity currents in a small ría: Estuary-amplified coastal edge waves?, *Estuarine Coastal Shelf Sci.*, *150*, 242–251, doi:10.1016/j.ecss.2014.04.019.

Webb, S. C., X. Zhang, and W. Crawford (1991), Infragravity waves in the deep ocean, *J. Geophys. Res.*, *96*(C2), 2723–2736, doi:10.1029/90JC02212.

Williams, M. E. (2014), Hydrodynamics and salt dispersion in intermittently closed bar-built estuaries, PhD thesis, Univ. of Calif., Berkeley, Calif.

Wolanski, E., D. Williams, S. Spagnol, and H. Chanson (2004), Undular tidal bore dynamics in the Daly Estuary, Northern Australia, *Estuarine Coastal Shelf Sci.*, *60*(4), 629–636, doi:10.1016/j.ecss.2004.03.001.